Journal of Materials Chemistry C

Visualizing transport in thiazole flanked isoindigo-based donor-acceptor polymer field-effect transistors

Journal:	*Journal of Materials Chemistry C*
Manuscript ID	TC-ART-06-2022-002748.R2
Article Type:	Paper
Date Submitted by the Author:	07-Sep-2022
Complete List of Authors:	Barron, John; University of Missouri, Physics Attar, Salahuddin; Texas A&M University at Qatar Bhattacharya, Payal; University of Missouri, Physics Yu, Ping; University of Missouri, Physics Al-Hashimi, Mohammed; Texas A&M University at Qatar Guha, Suchismita; University of Missouri, Physics

ARTICLE

Visualizing transport in thiazole flanked isoindigo-based donor-acceptor polymer field-effect transistors

Received 00th January 20xx,
Accepted 00th January 20xx

DOI: 10.1039/x0xx00000x

John Barron[a], Salahuddin Attar[b], Payal Bhattacharya[a], Ping Yu[a], Mohammed Al-Hashimi[b]*, and Suchismita Guha[a]†

Fluorination of donor-acceptor copolymers has been one strategy towards enhancing polymer coplanarity, increasing crystallinity, and improving charge transport mechanisms in organic devices. Herein, we report on the synthesis of thiazole flanked fluorinated isoindigo (IID) copolymers and demonstrate their field-effect transistor (FET) properties. The selenophene-substituted IID shows improved performance over the thiophene units. Different FET geometries were fabricated and tested. Top-gate FETs with varying dielectric layers showed n-type transport with electron carrier mobilities of the order of 10^{-2} cm^2/Vs and on/off ratio of 10^5. Along with improving the electronic properties, fluorination is an effective means of enhancing the nonlinear optical properties. We exploit this feature by observing the semiconductor-dielectric polarization induced by the applied electric field and the injected carriers. Time-resolved electric field-induced second harmonic generation method is used to visualize the carrier motion within the FET channel region, which gives an alternate estimate of the electron carrier mobility, free from contact resistance issues.

Introduction

The strong charge delocalization in donor-acceptor (D-A) copolymers continue to attract attention in electronic devices due to their versatility and tunability. Incorporating donor and acceptor chromophores in a polymer chain enables both p-type and n-type transport. Since the relative contribution of the electron-donating and -accepting components may be synthetically controlled, which in turn alters the electronic and optical properties, oligomers and polymers based on D-A moieties are attractive for applications in organic electronics. Several research groups have focussed on copolymers of diketopyrrolopyrrole due to their high carrier mobilities, and have demonstrated their application in organic field-effect transistors (FETs) and solar cells.[1-9] Isoindigo (IID) based electron acceptors have received less attention compared to other D-A copolymers, presumably due to their low charge carrier mobility. Some of the early work dates back to more than 10 years ago, where the optical and electrochemical properties of IID based polymers were found to be favourable for optoelectronic devices.[10] Since then, electron deficient IID units have been incorporated in solar cells,[11, 12] and their ambipolar nature has been exploited in p- and n-type FETs.[13-16] Furthermore, thiazole based materials are emerging as a viable route towards n-type or ambipolar properties in conjugated polymers.[17-19]

An approach for tuning the HOMO-LUMO gap along with facilitating solid state interactions is to replace the sulphur (S) atom in the five-membered ring with heavier atoms such as Se or Te.[20, 21] The size of the heteroatom dictates both the solubility and the size of the optical bandgap. Replacing S with Se in IIDs is seen to favourably enhance charge transport properties in FETs.[22] Fluorination of D-A moieties has been another strategy for improving the ambipolar nature of charge transport by lowering the LUMO level. Not only does fluorination enhance crystallinity, it promotes molecular orbital hybridization between the monomer units, resulting in planarization of the backbone.[23] Fluorinated benzothiadiazole based conjugated systems are shown to enhance the degree of coplanarity, leading to improved charge transport properties.[18, 24] Fluorinated IID polymers in FETs have shown electron mobilities upwards of 0.5 cm^2/Vs while maintaining a high hole mobility under ambient conditions.[13] Fluorination may also be exploited to enhance the dipole moment of the system for nonlinear optical properties,[25] which can be utilized for visualizing transport in FETs.

Most electrical measurements in organic FETs are plagued by contact resistance issues stemming from the energetic mismatch between the Fermi levels of the electrode material and the organic semiconductor. Other factors such as interface states, energetic disorder, and the nature of the dielectric layer also impact contact resistance, and can thus lead to the extraction of imprecise FET parameters. Several recent works have addressed mechanisms by which contact resistance may be reduced in organic FETs.[26-28] Nonlinear optical imaging

[a] Department of Physics and Astronomy, University of Missouri, Columbia, MO 65211, USA
[b] Department of Chemistry, Texas A&M University at Qatar, P.O. Box 23874, Doha, Qatar
Corresponding author E-mail: *mohammed.al-hashimi@tamu.edu; †guhas@missouri.edu

Electronic Supplementary Information (ESI) available: Synthesis of copolymers and device fabrication; Thermal properties; NMR results; EFISHG setup and results. See DOI: 10.1039/x0xx00000x

provides a platform for obtaining carrier mobilities in FETs, free from contact resistance issues.

In the late 1990s it was shown that the second-order nonlinear optical response in the presence of an electric field allowed mapping the charge distribution at the interface in Si-based metal oxide semiconductor devices.[29, 30] Since then, transient electric field-induced second harmonic generation (TR-EFISHG) methods, based on the third-order susceptibility, have provided a path for probing dynamic carrier motion in organic FETs. [31-33] For EFISHG to be realized, materials are not required to be non-centrosymmetric. Typical electric fields (~ 10^4 V/cm) applied as the parallel source-drain fields in FETs are adequate to break the symmetry, and if excited with light of frequency, ω, it results in the second harmonically generated light at 2ω. In TR-EFISHG, the carrier motion is indirectly probed by visualizing the movement of the dielectric polarization induced by the electric field of the moving carriers.

Here, we have synthesized thiazole flanked fluorinated isoindigo copolymers with thiophene (**P1**) and selenophene (**P2**) units and utilize them in different FET geometries. **P1** and **P2** show maxima in their absorption peaks around 620 nm, with a distinctive shoulder at 675 nm for **P1**. When used in bottom gate architectures with SiO_2 as the dielectric layer, both copolymers show n- and p-type transport, although with very low carrier mobilities. When using top gate architectures which utilize CYTOP as the dielectric layer, the **P2** copolymer shows an improved n-type transport compared with **P1**, with n-type carrier mobilities on the order of 10^{-2} cm^2/Vs. The use of poly (methyl methacrylate) (PMMA) as the dielectric in a top gate architecture further improves device performance. These top gate architectures predominantly show n-type behaviour. We have further carried out TR-EFISHG imaging from PMMA based **P2** FETs using an ultrafast laser (100 fs) system. The pulsed laser of wavelength 1280 nm, incident on the device using a microscope objective, is synchronized with the applied pulsed voltage (gate-source and drain-source), where the delay between the two pulses can be controlled. At different snapshots of the delay time, second harmonic generation images were acquired, representing the motion of carriers. The n-type carrier mobility extracted from these images is independent of the contact resistance and was found to be two orders of magnitude higher than the electrical measurements in some cases.

Experimental Methods

Synthesis

Monomer Synthesis. The synthetic route to monomer **M1** is demonstrated in **Scheme 1**. Stille coupling of 2 2-(tributylstannyl)thiazole with (E)-6,6'-dibromo-1,1'-bis(4-decyltetradecyl)-7,7'-difluoro-[3,3'-biindolinylidene]-2,2'-dione **1** afforded (E)-1,1'-bis(4-decyltetradecyl)-7,7'-difluoro-6,6'-di(thiazol-2-yl)-[3,3'-biindolinylidene]-2,2'-dione **2** as an brown solid in 95% yield. Brominating the electron deficient flanking thiazole units at the 2-position or 5-position pose significant challenges, thus often requiring long reaction times and producing low yields.[17, 34-36] Bromination of compound **2** using NBS or Br_2 did not give us the desired dibrominated product (Table S1, Supplementary Information). The di-bromination step was investigated under different conditions either producing very low quantity of the monobrominated compound **4** or the starting material was recovered. Subsequently, performing the dibromination reaction with molecular bromine in the presence of a weak base such as pyridine resulted in the formation of the desired dibrominated product (Table S2, Supplementary Information).

Polymer Synthesis. As shown in **Scheme 2,** copolymers **P1** and **P2** were prepared via microwave-assisted Stille coupling of **M1** with the 2,5-bis(trimethylstannyl)thiophene and 2,5-bis(trimethylstannyl)selenophene in chlorobenzene using Tetrakis(triphenylphosphine) palladium (0) as a catalyst. Both the polymers were precipitated in acidified methanol and purified via Soxhlet extraction with a sequence of refluxing methanol, acetone, and n-hexane. Finally, refluxing chloroform was used to extract the polymers. After removing the solvent, **P1** and **P2** were dissolved in chlorobenzene and reprecipitated in 50% acetone in methanol and isolated as black solids. Each of the polymers possessed adequate solubility in chlorinated solvents such as chloroform and chlorobenzene. Gel permeation chromatography was utilized to determine the polydispersity index (Đ) and the number-average molecular weight (M_n). For this, a chlorobenzene solution at 85 °C was used with polystyrene standards as the calibrants. The M_n of homopolymers **P1** and **P2** were measured to be 90 and 29 kDa, respectively, with a narrow Đ in the range of 1.8-2.0. **Table 1** summarizes the physical, structural, and optical properties of **P1** and **P2**.

FET Fabrication

The FETs were fabricated using staggered architectures, either as a bottom gate and top contact (BGTC) or a top gate and bottom contact (TGBC). The former architecture was made utilizing a silicon substrate with heavily p-doped Si++ and a 200 nm SiO_2 oxide layer acting as the dielectric layer. The latter architecture was made using either CYTOP or PMMA as the top gate dielectric. The contacts themselves were patterned to make four devices per substrate, which had a 1000 µm channel width and four different lengths: 50 µm, 75 µm, 100 µm, and 125 µm. Details of the fabrication process are included in the Supplementary Information.

ARTICLE

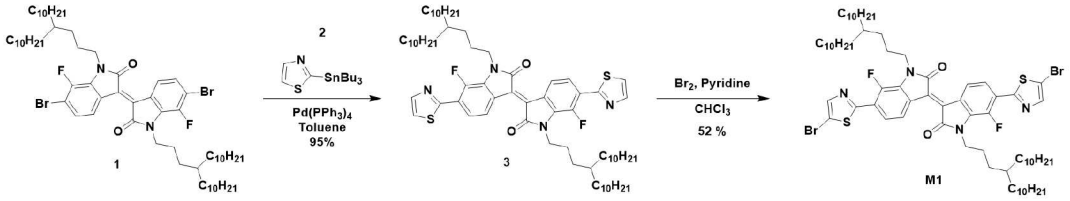

Scheme 1 Synthetic route to monomer **M1**.

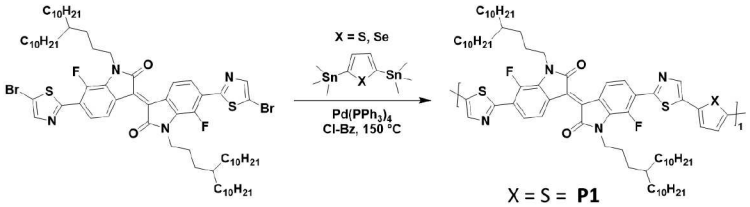

Scheme 2 Synthesis of copolymers **P1** and **P2**.

Table 1. Electrochemical, optical, thermal, AFM and XRD parameters of copolymers **P1** and **P2** as well as their molecular weights.*

	Mn (*kDa*)	*Đ*	*Td* (*°C*)	λ_{max}^{sol} *(nm)*	λ_{max}^{film} *(nm)*	*HOMO (eV)*	*LUMO (eV)*	E_g^{el} *(eV)*	E_g^{opt} *(eV)*	*Lamelar d (Å)*	*π-π d (Å)*	*RMS (nm)*
P1	90	1.8	397	631, 672	623, 675	-5.70	-3.84	1.86	1.66	23.47	3.62	4.33
P2	29	2.0	327	628	619	-5.56	-3.74	1.82	1.60	25.37	3.88	3.36

*Details of how these properties were determined are provided in the Supplementary Information.

Electrical Characterization

The electrical characteristics of the FET devices were measured using Keithley 236 and 2400 sourcemeters and a LabView program. The output characteristics, which are determined by sweeping the source-drain bias (V_{DS}), produce a current (I_D) which demonstrates the linear and saturation regimes of device operation for a given gate-source bias (V_{GS}). The transfer measurements, which are determined by sweeping V_{GS} while holding V_{DS} constant, produces a curve which reflects the operation of the FET device. The biases for the transfer measurement are selected based on the results of the output characteristics to ensure that the device is operating in the saturation regime. From the results of the transfer measurement, pertinent device characteristics including the charge carrier mobility (μ), the on/off ratio, and threshold voltage (V_{th}) were calculated. The saturation region of the transfer characteristics was used to extract μ. With C_i being the dielectric capacitance, L the channel length, and W the channel width, the saturation region $\mu = (2L/WC_i)(\partial\sqrt{I_D}/\partial V_{GS})^2$.

All measurements were performed under ambient conditions. For the BGTC architecture devices in which the semiconductor is exposed to atmosphere, a flow of nitrogen gas was applied over the device during measurement to reduce the influence of oxygen on deteriorating the channel. For the TGBC architecture devices, the CYTOP or PMMA acted to encapsulate the semiconductor, removing any influence from the atmosphere on the channel.

TR-EFISHG

The TR-EFISHG experiments were conducted with an excitation wavelength of 1280 nm from an optical parametric amplifier (TOPAS) using a regenerative amplifier (Spitfire Ace, Spectra Physics) with a repetition rate of 1 kHz, pulse duration of 100 fs, and seeded by a Ti-Sapphire laser (Mai Tai, Spectra

Physics). The group velocity dispersion due to the microscopic objective (50x) and other optical components was minimized using a prism compressor unit. A beam expander was placed before the microscopic objective to ensure that the entire channel region of the FET was illuminated. The SHG image was collected by an EMCCD camera (Photometrics Evolve 512) by placing a band pass filter (BG39) for removing the fundamental IR component and a band pass filter of 650 nm (± 40 nm) for allowing the SHG and further rejecting other wavelength components. A pulsed voltage (in the saturation region) of 1 kHz and amplitude of 40 V was applied to the drain-source and gate source contacts (V_{GS}=V_{DS}). The time delay between the voltage pulse and the laser pulse was achieved by a pulse delay generator (TOMBAK, AlphaNov). A schematic of the setup is shown in the Supplementary Information.

Results and discussion

Optical and electrochemical properties

Thin films of **P1** and **P2** were fabricated and measured using XRD in order to analyse the relationship between the chemical structure of the copolymers and their crystallinity behaviour. The lamellar/π-π stacking d-spacing values are summarized in **Table 1** and details are provided in the Supplementary Information.

The ultraviolet-visible (UV-vis) absorption spectra were obtained from both solution and thin films of **P1** and **P2** as shown in **Fig. 1**. The copolymers were dissolved in chlorobenzene. The backbone flexibility of the donor unit results in the smearing of the vibronic peaks, especially in **P2**. This is seen for lower concentrations as well (see Supplementary Information). The optical and electrochemical properties are detailed in **Table 1**. Both **P1** and **P2** in solution display a HOMO-LUMO absorption band represented by n-π* transitions in the visible region peaking at between 600 - 700 nm, while the π-π* energy bands absorb around 450 nm. From the solution to the solid state, **P1** and **P2** show a slight blue shift and broadening of the maximum absorbance peak (λ_{max}) from 631 nm to 623 nm and 628 nm to 619 nm, respectively, indicating a similar optical behaviour upon changing the heteroatom from S to Se. The onsets of the absorption spectra in the thin films were used to calculate the optical energy band gaps (E_g^{opt}) of **P1** and **P2,** which are 1.66 and 1.60 eV, respectively. This trend of lowering the bandgap energy upon selenophene substitution is also observed in the frontier molecular orbital energy levels and band gaps (E_g^{el}) derived from cyclic voltammetry. The HOMO and LUMO level are raised from -5.70 and -3.84 to -5.56 and -3.74 eV, respectively, from thiophene to selenophene substituents in the polymeric backbone.

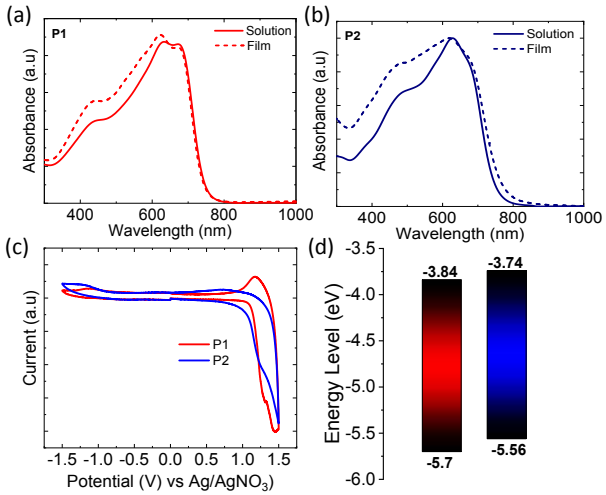

Fig. 1 UV-vis absorption spectra in chlorobenzene solutions and as thin film for **P1** (a) and **P2** (b). (c) Cyclic voltammetry and (d) HOMO-LUMO levels for **P1** (red) and **P2** (blue).

FET characteristics

The **P1** and **P2** semiconductors were initially used in BGTC FET architectures, which made use of silicon as the substrate with a heavily doped side acting as the device gate and 200 nm of SiO_2 acting as the dielectric layer to separate the gate from the semiconducting channel. A SAM layer (OTS) was also applied on the SiO_2 layer to alter its surface energy and improve film formation of the spin-coated semiconductor. The device architectures, results, and details of the fabrication steps are included in Supplementary Information. Devices utilizing this architecture were measured under a stream of nitrogen gas to avoid interactions from the ambient atmosphere with the semiconductor during operation.

In the BGTC architecture, both **P1** and **P2** exhibited ambipolar behaviour. Comparing their performance (Fig. S5), **P1** demonstrates comparable p-type and n-type behaviour with average mobilities of 1.6 x 10^{-6} cm^2/Vs and 1.2 x 10^{-6} cm^2/Vs, respectively. In contrast, **P2** shows a clear preference towards n-type behaviour with an average mobility of 1.2 x 10^{-4} cm^2/Vs, which is almost two orders of magnitude higher than its average p-type mobility of 7.6 x 10^{-6} cm^2/Vs. As seen below, the top-gate architecture devices show an improved FET performance.

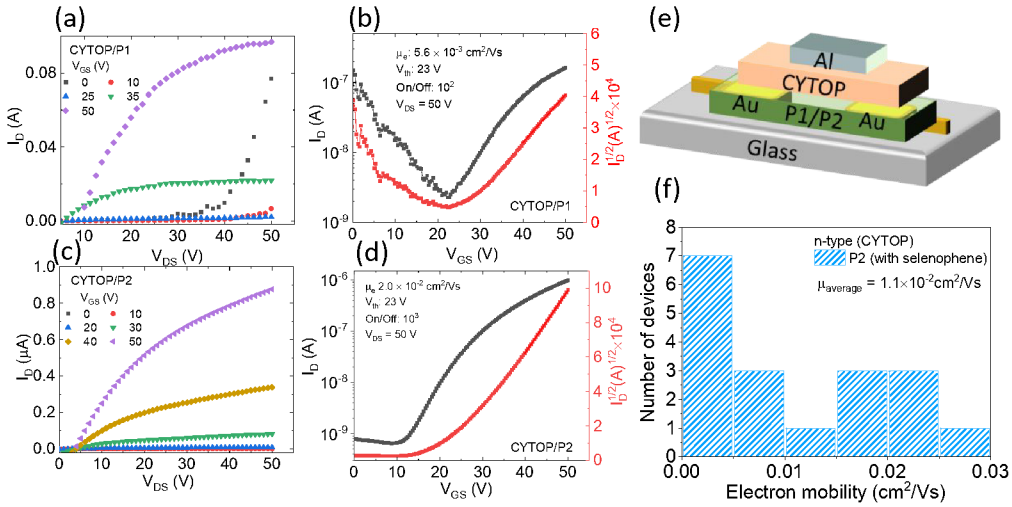

Fig. 2 (a) – (d) Output and transfer characteristics of top-gate (CYTOP)-bottom contact **P1** and **P2** FETs. The **P1** FET had W = 1000 μm, L = 125 μm, and the **P2** FET had W = 1000 μm, L = 50 μm. (e) Schematic of the device architecture. (f) Histogram of electron mobilities from top-gate **P2** FETs.

Top-gate-bottom contact FET characteristics

Several other recent works which utilize IID polymers in FET devices have made use of TGBC architectures.[13, 16, 37, 38] Like the BGTC structure used before, these staggered architectures have the benefit of allowing for better charge injection between the source-drain contacts and the semiconductor and are preferred for studying the ambipolar and n-type behaviour of these materials.[13, 39] The TGBC architecture has the added benefit of encapsulating the semiconductor layer from external influences of the atmosphere, allowing for measurement under ambient conditions.

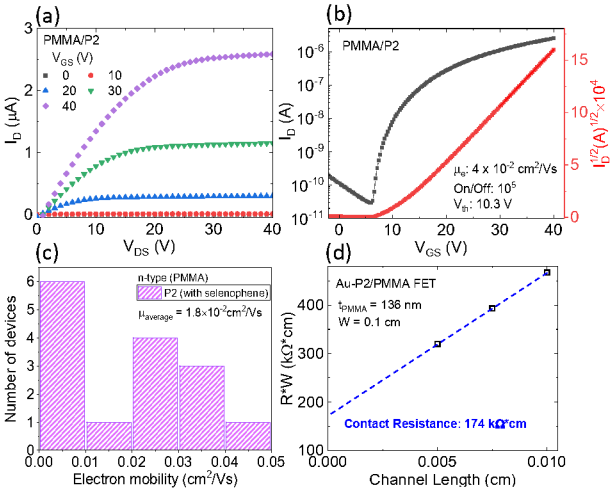

Fig. 3. (a), (b) Output and transfer characteristics of top-gate (PMMA)-bottom contact P2 FET (with W = 1000 μm, L = 100 μm). (c) Histogram of electron mobilities from top-gate (PMMA) P2 FETs. (d) Contact resistance estimation. The product of the channel width and total resistance versus channel length for a top gate (PMMA) P2 FET.

CYTOP was initially used in fabricating TGBC devices with **P1** and **P2**; the general architecture is shown in **Fig. 2** (e). **P1** in this architecture signals a weak ambipolar nature; however, as shown in the Supplementary Information, the leakage current is high with CYTOP as the dielectric. **P2** demonstrated exclusively n-type behaviour in the TGBC architectures. **Fig. 2** (b) and (d) demonstrate the transfer characteristics for **P1** and **P2** FETs operating in the saturation regime, respectively. The average mobility and on/off ratio for the **P2** devices were an order of magnitude higher than that of the **P1** devices, while both sets of devices had comparable threshold voltage values. A histogram of mobilities from **P2** FETs is shown in **Fig. 2** (f) with an average electron mobility of 1.1×10^{-2} cm^2/Vs.

To reduce the gate leakage current, top gate **P1** and **P2** FETs with PMMA were also fabricated. Results from **P1** are presented in Supplementary Information. As shown in **Fig. 3**, the **P2** FETs display a higher on/off ratio (10^5). By comparing the output curves in **Figs. 2** (c) and **3** (a), it is evident that there is higher leakage in the CYTOP/**P2** FET. There is a slight improvement in the carrier mobility upon using PMMA but the order is the same as the CYTOP devices. **Fig. 3** (c) shows a histogram of the electron mobilities from 15 devices. **Fig. 3** (d) plots the contact resistance from one such PMMA/**P2** FET. The commonly-used transmission line method (TLM) was utilized to calculate the contact resistance normalized with *W* (from the linear region of the output curve), based on the following relationship:

$$RW = R_C W + \frac{L}{\mu_{eff} C_i (V_{GS} - V_{Th})}, \qquad (1)$$

where *R* is the total resistance, R_C is contact resistance, and μ_{eff} is the effective mobility which in principle is free from

contact resistance.[40] Although there could be differences between the contact resistance obtained from the normal linear region and the saturation region,[41] we use the slope from **Fig. 3** (d) to estimate μ_{eff} for a rough comparison with the above electrical measurements and the EFISHG mobility in the next section. For V_{GS} = 50 V, where V_{Th} varies between 7 V– 9 V, μ_{eff} = 0.06 cm²/Vs. It should, however, be noted that since V_{Th} varies from device to device, the TLM method is not completely reliable to obtain contact-free carrier mobility; a better electrical method is the gated four-probe method.[42] The average value of the contact resistance from the **P2** devices is 170 kΩ cm.

In summarizing the electrical measurements, we fabricated both BGTC (with SiO_2 as the dielectric layer) and TGBC (either with CYTOP or PMMA) FETs with the two copolymers, **P1** and **P2**. A clear improvement is seen in the TGBC devices. The n-type characteristics in both **P1** and **P2** are strongly enhanced in TGBC FETs, similar to what has been observed in other D-A systems such as benzodipyrrolidone-based copolymers.[43] Moreover, **P2** shows an order of magnitude higher FET carrier mobility compared with **P1**.

To gain further insight into the carrier motion, in particular to observe whether n-type is the predominant behaviour, and to obtain a better estimate of the carrier mobility, free from contact resistance, we have obtained TR-EFISHG images from top-gate PMMA/**P2** FETs.

TR-EFISHG imaging from P2 FETs

We used top-gate (PMMA) **P2** FETs for TR-EFISHG imaging. **Fig. 4** (a) shows a schematic of the device where a pulsed voltage is applied to the gate and the drain. Since the EFISHG signal depends on the third order nonlinear optical susceptibility ($\chi^{(3)}$), the incident wavelength should be appropriately chosen. $\chi^{(3)}$ in **P2** is seen to be the highest at 1280 nm (see Supplementary Information). The incident light was s-polarized (perpendicular to the direction of the application of V_{DS}). This geometry yields the maximum SHG intensity due to the selection rule.[44] The fundamental light (1280 nm) is incident from the glass interface and the SHG light is collected from the same side. The incident light with a repetition rate of 1 kHz is synchronized with the applied pulsed voltage, where the time delay (τ) between the two signals can be changed, as shown in **Fig. 4** (b). At t = τ, the injected carriers distribute along the channel of the FET. Prior to the EFISHG measurements, transfer characteristics were measured from the same device, shown in **Fig. 4** (c). The carrier mobility determined from the saturation region yields a value of 1.4×10^{-2} cm²/Vs.

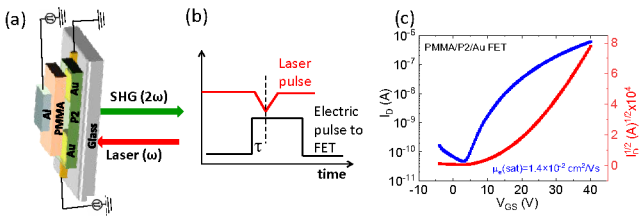

Fig. 4 (a) Schematic of the top-gate (PMMA) P2 FET with the electrical connections for TR-EFISHG imaging. A fundamental laser wavelength of 1280 nm (80 fs) at a repetition rate of 1 kHz was incident on the sample. (b) The pulsed laser source is synchronized with an applied pulsed voltage of 40 V with a time delay of τ. (c) Transfer characteristics from the FET used for the measurement of TR-EFISHG.

Fig. 5 (a) – (f) shows the TR-EFISHG images from a PMMA/**P2** FET with L = 50 μm. Snapshots at delay times of 0 μs, 0.5 μs, 1.0 μs, 1.5 μs, and 2.0 μs are shown. The plot profiles are shown below the images. In each case, a pulsed voltage of V_{DS} = V_{GS} = 40 V was applied. At 0 μs, a clear SHG signal from the electrodes is observed. This is mainly the EFISHG signal due to the applied field (Laplace contribution). As the delay time is increased between the voltage and the laser pulse, the intensity of the SHG signal changes due to a movement of the induced polarization, which represents carrier motion. Once the carriers are injected, along with the Laplace field, a Poisson field due to the space-charge field is also setup. Since interfaces break the symmetry, a very weak SH signal is observed, which may be responsible for the differences in the background of the various images. No movement of induced polarization was observed in the TR-EFISHG images upon reversing the polarity of the applied voltage, suggesting that the PMMA/**P2** FET demonstrates only n-type transport.

At 0.5 μs, a polarization cloud appears near the drain electrode (depicted by the white arrow) (**Fig. 5** (b)), which is then seen to move towards the source electrode in subsequent images. The position was measured by noting the location of the front edge of the wavefront in the actual images. In each case, the position (L) was noted with respect to the drain electrode. The position of the induced polarization is marked by the red arrow in the plot profile. Using a Gaussian peak fit to the induced polarization, we estimate an error bar of ± 2 μm to the absolute position of the polarization wavefront within the channel. Since the injected charges are electrons, the induced polarization moves from the drain to the source contact. This is in the opposite direction compared to p-type FETs such as in pentacene FETs.[33] By the time τ = 2.0 μs, the transit of the carriers (or rather the induced polarization which is now closer to the source electrode) is almost over. At this time, the Poisson field, which negates the Laplace field, will be the largest and one would expect the SHG signal to weaken as observed in **Fig. 5** (e) (see the plot profile).

To estimate the carrier mobility, we describe the carrier transport as the drift in the average electric field (V/L) at a constant velocity. A similar model for extracting carrier mobilities from TR-EFISHG images has been used in the literature, which assumes a uniform electric field.[44] Since the threshold voltage for the FET is substantial (14 V) and so as to not overestimate the carrier mobility, we use the drift model of a two-terminal device for the transit time, t_{tr}:

$$t_{tr} = \frac{1L^2}{\mu V}, \qquad (2)$$

where *V'* is the applied drain-source voltage, *L* is the channel length and μ is the carrier mobility. From the slope of the line of delay time versus L^2, and using the applied voltage of 40 V (**Fig. 5** (f)), we obtain $\mu = 0.25 \pm 0.025$ cm^2/Vs. We note this mobility is almost an order of magnitude higher than what is obtained from the electrical measurements.

Since the EFISHG signal is collected through glass (**Fig. 4** (a)), there is some amount of spread in the induced polarization wavefront. An example of TR-EFISHG from an aged **P2** (same batch as is in **Fig. 5**) FET, measured after 5 months of fabrication, is shown in the Supplementary Information. Here, the the overall performance of the PMMA/**P2** FET had diminished, and μ_e yields 2.7×10^{-3} cm^2/Vs when calculated from the transfer characteristics operating in the saturation regime. By changing the delay between the laser and the voltage pulse, the induced polarization which depicts carrier motion is again seen to move from the drain to the source electrode. μ_e obtained from the TR-EFISHG images is 0.155 cm^2/Vs, which is the same order of magnitude as the pristine samples, further demonstrating that EFISHG images give a reliable estimate of carrier mobilities even upon any degradation of the metal-semiconductor interface.

A detailed study on the effect of molecular weight on device performance in Se-based IIDs is underway. Preliminary results from **P2** (with Mn>50 kDa) FETs indicate an order of magnitude lower μ_e compared to **Fig. 3**. A set of TR-EFISHG images from such a device is shown in Supplementary Information, further confirming the reliability of the technique across a wide range of electrical performance. Our results, therefore, suggest that by reducing the contact resistance, for example by treating the Au electrodes by a SAM layer or by contact doping, it is possible to achieve improved charge injection and electron carrier mobilities upwards of 0.2 cm^2/Vs in selenophene substituted IID copolymer.

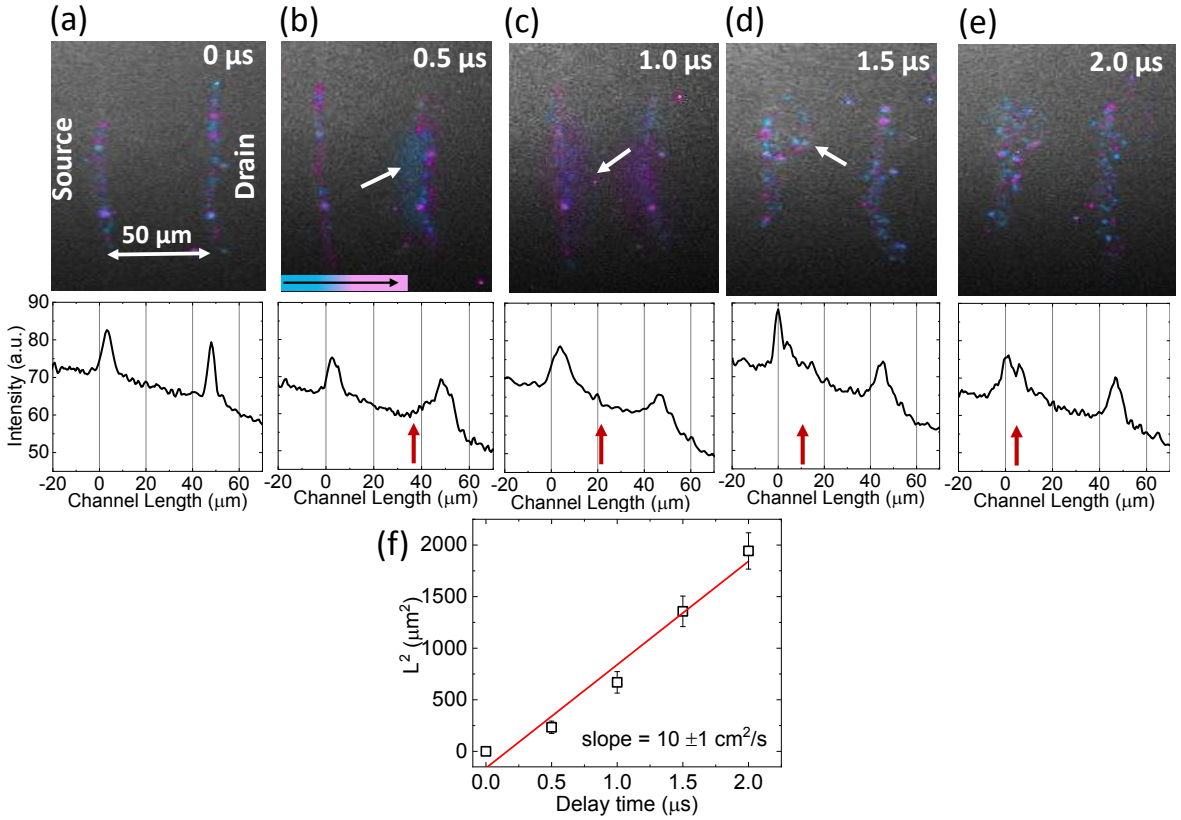

Fig. 5 (a) – (e) Snapshots of the EFISHG signal moving across the channel region of a PMMA/**P2** FET at four different delay times. The SHG intensity plot profile is shown below the images in each case. The red arrow in the plot profile and the white arrows in the actual images depict the position of the induced polarization. The colour bar in (b) depicts increasing SHG intensity. (f) The position of the carrier front as a function of the delay (transit) time, satisfying eq. (2).

ARTICLE

Conclusions

In conclusion, fluorinated IID based D-A copolymers provide an opportunity for tuning the HOMO-LUMO gap by replacing S in the five-membered ring with heavier atoms. Selenophene-based thiazole flanked IID is seen to show improved charge transport properties in FET architectures compared with its thiophene counterpart. **P1** and **P2** top-gate FETs predominantly show n-type characteristics. Using TR-EFISHG techniques, the carrier motion can be imaged by observing the movement of the injected charge carriers within the FET channel, providing an alternate mechanism for obtaining the carrier mobility. Such measurements yield μ_e to be higher than 0.2 cm^2/Vs in **P2** FETs. This works opens up the prospect of substitutions other than Se in fluorinated IIDs along with optimized metal-semiconductor contacts for improved charge-transport properties.

Author Contributions

S. Attar and M. Al-Hashimi carried out the synthesis of the copolymers and the optical and electrochemical measurements. J. Barron and S. Guha conceived the transistor experiments and carried out the analysis. J. Barron fabricated the FETs and was involved with the electrical measurements. P. Yu, P. Bhattacharya, and S. Guha set up the TR-EFISHG capabilities. P. Bhattacharya measured and analysed the EFISHG images. All authors discussed and contributed to the manuscript. S. Guha, J. Barron, and M. Al-Hashimi wrote and edited the manuscript.

Conflicts of interest

There are no conflicts to declare.

Acknowledgements

We acknowledge the support of this work through the U.S. National Science Foundation (NSF) under Grant No. ECCS-1707588 and ECCS-1872846, and Qatar National Research Fund (QNRF) and the National Priorities Research Program (project number NPRP12S-0304-190227). Dr. Wubulikaisimu Yiming is acknowledged for the help in collecting the AFM data.

Notes and references

1. H. W. Lee, H. S. Kim, D. Kim, M. Yoon, J. Lee and D.-H. Hwang, *Chem. Mater.*, 2022, **34**, 314-324.
2. C. Kanimozhi, N. Yaacobi-Gross, K. W. Chou, A. Amassian, T. D. Anthopoulos and S. Patil, *J. Am. Chem. Soc.*, 2012, **134**, 16532-16535.
3. J. Li, Y. Zhao, H. S. Tan, Y. Guo, C.-A. Di, G. Yu, Y. Liu, M. Lin, S. H. Lim, Y. Zhou, H. Su and B. S. Ong, *Sci. Rep.*, 2012, **2**, 754.
4. P. Sonar, S. P. Singh, Y. Li, M. S. Soh and A. Dodabalapur, *Adv. Mater.*, 2010, **22**, 5409-5413.
5. Y. Zhang, C. Kim, J. Lin and T.-Q. Nguyen, *Adv. Funct. Mater.*, 2012, **22**, 97-105.
6. D. Adil, C. Kanimozhi, N. Ukah, K. Paudel, S. Patil and S. Guha, *ACS Appl. Mater. Interfaces*, 2011, **3**, 1463-1471.
7. T. Mukhopadhyay, B. Puttaraju, S. P. Senanayak, A. Sadhanala, R. Friend, H. A. Faber, T. D. Anthopoulos, U. Salzner, A. Meyer and S. Patil, *ACS Appl. Mater. Interfaces*, 2016, **8**, 25415-25427.
8. J. Liu, Y. Sun, P. Moonsin, M. Kuik, C. M. Proctor, J. Lin, B. B. Hsu, V. Promarak, A. J. Heeger and T.-Q. Nguyen, *Adv. Mater.*, 2013, **25**, 5898-5903.
9. B. Chen, Y. Yang, P. Cheng, X. Chen, X. Zhan and J. Qin, *J. Mater. Chem. A*, 2015, **3**, 6894-6900.
10. R. Stalder, J. Mei and J. R. Reynolds, *Macromolecules*, 2010, **43**, 8348-8352.
11. Z. Ma, E. Wang, M. E. Jarvid, P. Henriksson, O. Inganäs, F. Zhang and M. R. Andersson, *J. Mater. Chem.*, 2012, **22**, 2306-2314.
12. E. Wang, Z. Ma, Z. Zhang, K. Vandewal, P. Henriksson, O. Inganäs, F. Zhang and M. R. Andersson, *J. Am. Chem. Soc.*, 2011, **133**, 14244-14247.
13. T. Lei, J.-H. Dou, Z.-J. Ma, C.-H. Yao, C.-J. Liu, J.-Y. Wang and J. Pei, *J. Am. Chem. Soc.*, 2012, **134**, 20025-20028.
14. E.-S. Shin, Y. H. Ha, E. Gann, Y.-J. Lee, S.-K. Kwon, C. R. McNeill, Y.-Y. Noh and Y.-H. Kim, *ACS Appl. Mater. Interfaces*, 2018, **10**, 13774-13782.
15. S. E. Yoon, S. J. Shin, S. Y. Lee, G. G. Jeon, H. Kang, H. Seo, J. Zheng and J. H. Kim, *ACS Appl. Polym. Mater.*, 2020, **2**, 2729-2735.
16. J. Yang, Z. Zhao, H. Geng, C. Cheng, J. Chen, Y. Sun, L. Shi, Y. Yi, Z. Shuai, Y. Guo, S. Wang and Y. Liu, *Adv. Mater.*, 2017, **29**, 1702115.
17. Y. Shi, H. Guo, M. Qin, Y. Wang, J. Zhao, H. Sun, H. Wang, Y. Wang, X. Zhou, A. Facchetti, X. Lu, M. Zhou and X. Guo, *Chem. Mater.*, 2018, **30**, 7988-8001.
18. M. Barłóg, X. Zhang, I. Kulai, D. S. Yang, D. N. Sredojevic, A. Sil, X. Ji, K. S. M. Salih, H. S. Bazzi, H. Bronstein, L. Fang, J. Kim, T. J. Marks, X. Guo and M. Al-Hashimi, *Chem. Mater.*, 2019, **31**, 9488-9496.
19. S. Dey, S. Attar, E. F. Manley, S. Moncho, E. N. Brothers, H. S. Bazzi, H. Bronstein, T. J. Marks, M. Heeney, B. C. Schroeder and M. Al-Hashimi, *ACS Appl. Mater. Interfaces*, 2021, **13**, 41094-41101.

20. M. Al-Hashimi, Y. Han, J. Smith, H. S. Bazzi, S. Y. A. Alqaradawi, S. E. Watkins, T. D. Anthopoulos and M. Heeney, *Chem. Sci.*, 2016, **7**, 1093-1099.
21. D. Patra, J. Lee, S. Dey, J. Lee, A. J. Kalin, A. Putta, Z. Fei, T. McCarthy-Ward, H. S. Bazzi, L. Fang, M. Heeney, M.-H. Yoon and M. Al-Hashimi, *Macromolecules*, 2018, **51**, 6076-6084.
22. K. H. Park, K. H. Cheon, Y.-J. Lee, D. S. Chung, S.-K. Kwon and Y.-H. Kim, *Chem. Comm.*, 2015, **51**, 8120-8122.
23. S. Holliday, J. E. Donaghey and I. McCulloch, *Chem. Mater.*, 2014, **26**, 647-663.
24. M. Barłóg, I. Kulai, X. Ji, N. Bhuvanesh, S. Dey, E. P. Sliwinski, H. S. Bazzi, L. Fang and M. Al-Hashimi, *Org. Chem. Front.*, 2019, **6**, 780-790.
25. S. Khanra, S. V. Vassiliades, W. A. Alves, K. Yang, R. Glaser, K. Ghosh, P. Bhattacharya, P. Yu and S. Guha, *AIP Adv.*, 2019, **9**, 115202.
26. J. W. Borchert, B. Peng, F. Letzkus, J. N. Burghartz, P. K. L. Chan, K. Zojer, S. Ludwigs and H. Klauk, *Nat. Comm.*, 2019, **10**, 1119.
27. Z. A. Lamport, K. J. Barth, H. Lee, E. Gann, S. Engmann, H. Chen, M. Guthold, I. McCulloch, J. E. Anthony, L. J. Richter, D. M. DeLongchamp and O. D. Jurchescu, *Nat. Comm.*, 2018, **9**, 5130.
28. M. Waldrip, O. D. Jurchescu, D. J. Gundlach and E. G. Bittle, *Adv. Funct. Mater.*, 2020, **30**, 1904576.
29. O. A. Aktsipetrov, A. A. Fedyanin, E. D. Mishina, A. N. Rubtsov, C. W. van Hasselt, M. A. C. Devillers and T. Rasing, *Phys. Rev. B*, 1996, **54**, 1825-1832.
30. O. A. Aktsipetrov, A. A. Fedyanin, A. V. Melnikov, E. D. Mishina, A. N. Rubtsov, M. H. Anderson, P. T. Wilson, M. ter Beek, X. F. Hu, J. I. Dadap and M. C. Downer, *Phys. Rev. B*, 1999, **60**, 8924-8938.
31. T. Manaka, E. Lim, R. Tamura and M. Iwamoto, *Nat. Photon.*, 2007, **1**, 581-584.
32. M. Iwamoto, T. Manaka and D. Taguchi, *Jpn. J. Appl. Phys.*, 2014, **53**, 100101.
33. M. Iwamoto, T. Manaka and D. Taguchi, *J. Phys. D: Appl. Phys*, 2015, **48**, 373001.
34. S. Wang, H. Sun, T. Erdmann, G. Wang, D. Fazzi, U. Lappan, Y. Puttisong, Z. Chen, M. Berggren, X. Crispin, A. Kiriy, B. Voit, T. J. Marks, S. Fabiano and A. Facchetti, *Adv. Mater.*, 2018, **30**, 1801898.
35. B. Carsten, J. M. Szarko, L. Lu, H. J. Son, F. He, Y. Y. Botros, L. X. Chen and L. Yu, *Macromolecules*, 2012, **45**, 6390-6395.
36. W. Li, K. H. Hendriks, A. Furlan, M. M. Wienk and R. A. J. Janssen, *J. Am. Chem. Soc.*, 2015, **137**, 2231-2234.
37. Y. Gao, Y. Deng, H. Tian, J. Zhang, D. Yan, Y. Geng and F. Wang, *Adv. Mater.*, 2017, **29**, 1606217.
38. Y. Jiang, J. Chen, Y. Sun, Q. Li, Z. Cai, J. Li, Y. Guo, W. Hu and Y. Liu, *Adv. Mater.*, 2019, **31**, 1805761.
39. H. Klauk, *Chem. Soc. Rev.*, 2010, **39**, 2643-2666.
40. Y. Xu, Y. Li, S. Li, F. Balestra, G. Ghibaudo, W. Li, Y.-F. Lin, H. Sun, J. Wan, X. Wang, Y. Guo, Y. Shi and Y.-Y. Noh, *Adv. Funct. Mater.*, 2020, **30**, 1904508.
41. M. Imakawa, K. Sawabe, Y. Yomogida, Y. Iwasa and T. Takenobu, *Appl. Phys. Lett.*, 2011, **99**, 233301.
42. C. Rolin, E. Kang, J.-H. Lee, G. Borghs, P. Heremans and J. Genoe, *Nat. Comm.*, 2017, **8**, 14975.
43. J. W. Rumer, S. Rossbauer, M. Planells, S. E. Watkins, T. D. Anthopoulos and I. McCulloch, *J. Mater. Chem. C*, 2014, **2**, 8822-8828.
44. T. Manaka and M. Iwamoto, *Light Sci. Appl.*, 2016, **5**, e16040-e16040.